American Mineralogist, Volume 83, pages 1454–1468, 1998

Sulfur isotope variability in biogenic pyrite: Reflections of heterogeneous bacterial colonization?

MATTHEW J. KOHN,[1,*] LEE R. RICIPUTI,[2] DEBRA STAKES,[3] and DANIEL L. ORANGE[4]

[1]Institute for Geophysics and Planetary Physics, Lawrence Livermore National Laboratory, Livermore, California 94550, U.S.A.
[2]Chemical and Analytical Sciences Division, Oak Ridge National Laboratory, Oak Ridge, Tennessee 37831-6365, U.S.A.
[3]Monterey Bay Aquarium Research Institute, P.O. Box 628, Moss Landing, California 95039-0628, U.S.A.
[4]Department of Earth Sciences, University of California at Santa Cruz, Santa Cruz, California 95062, U.S.A.

ABSTRACT

The top 20 cm of sediments at active cold seeps in Monterey Bay, coastal California, contain framboidal pyrite that occurs as infillings and pseudomorphs of the chambers of the tests of foraminifera and rarely as irregularly shaped grains. Sulfur isotope compositions obtained with the ion microprobe show depletions in ^{34}S ($\delta^{34}S = -41$ to $-5‰$, CDT), and large variations both within and among these pyrite grains. Intergranular differences in $\delta^{34}S$ values in the same sediment are as large as 35‰, and intragranular zoning reaches 15‰. Zoning is regular in some grains, with systematic isotope changes from core to rim or from one foraminiferal chamber to another, but irregular in others. The regular zoning is consistent with an increase in ^{34}S through time. Backscattered-electron imaging reveals three types of pyrite: isolated framboids in a porous aggregation ("PF-pyrite"), agglomerated framboids with cementing interstitial pyrite ("F+I-pyrite"), and recrystallized pyrite with isolated relicts of framboids ("RF-pyrite"). In individual grains, RF-pyrite cores grade into F+I-pyrite toward grain rims, and F+I-pyrite grades into PF-pyrite at the grain edges. These textures are consistent with a paragenetic sequence whereby framboids first agglomerate (PF-pyrite), then cement (F+I-pyrite), and finally recrystallize (RF-pyrite). The $\delta^{34}S$ values of RF-pyrite are generally lower than that of F+I-pyrite; if the paragenetic sequence is correct, then this trend parallels the regular core-rim isotopic zoning observed in some grains. The implied increase in $\delta^{34}S$ with time is consistent with Rayleigh fractionation of sulfur in a closed system. Bacteria are intimately involved in the production of pyrite from our samples, and heterogeneous colonization by bacteria provides a simple explanation for the sulfur isotope heterogeneity among and within grains: The foraminifera provide open space for colonization and local nutrients for bacterial growth, whereas the cell walls of the bacteria may provide a local nucleation site for sulfides. If so, then initial colonization is reflected in lower $\delta^{34}S$ values, whereas later bacterial emigration to other foraminifera chambers is indicated by higher $\delta^{34}S$ values.

INTRODUCTION

Sulfur isotope compositions of iron sulfides have been instrumental in elucidating the role of microorganisms in the precipitation of minerals. For example, low (<5‰) and variable $\delta^{34}S$ values in 2.75 Ga pyrite have been used to argue for the presence of sulfate-reducing bacteria by the late Archean on Earth (Goodwin et al. 1976; Thode and Goodwin 1983), whereas high $\delta^{34}S$ values for pyrite are believed to indicate a non-biological origin for possibly low-temperature minerals in Martian meteorites (Shearer et al. 1996; Greenwood et al. 1997). In parallel with the development of detailed chemical descriptions of how sulfides may form in sediments (e.g., Berner 1970, 1984; Sweeney and Kaplan 1973; Morse et al. 1987; Schoonen and Barnes 1991a, 1991b; Wilkin and Barnes 1996; Rickard 1997), dramatic improvements have occurred in the analytical capabilities for measuring sulfur isotopes in solid phases. Within the last 10 years, secondary ion mass spectrometry (SIMS) or the "ion microprobe" has taken a lead role in rapidly and precisely resolving sulfur isotope heterogeneities at a ~10 μm scale (e.g., Deloule et al. 1986; Eldridge et al. 1987; Graham and Valley 1991; Paterson et al. 1997). Indeed, in situ microanalysis now allows renewed examination of the complex biological and chemical interplay that occurs in sediments during sulfide precipitation.

In this paper, we present new sulfur isotope data for pyrites obtained for sediments of Monterey Bay, coastal California, U.S.A. The ion microprobe was used to maximize spatial resolution, with a view toward using the data to obtain new insights into the possible chemical and physical controls on authigenic pyrite precipitation. Our

* E-mail: mjk@llnl.gov

0003–004X/98/1112–1454$05.00

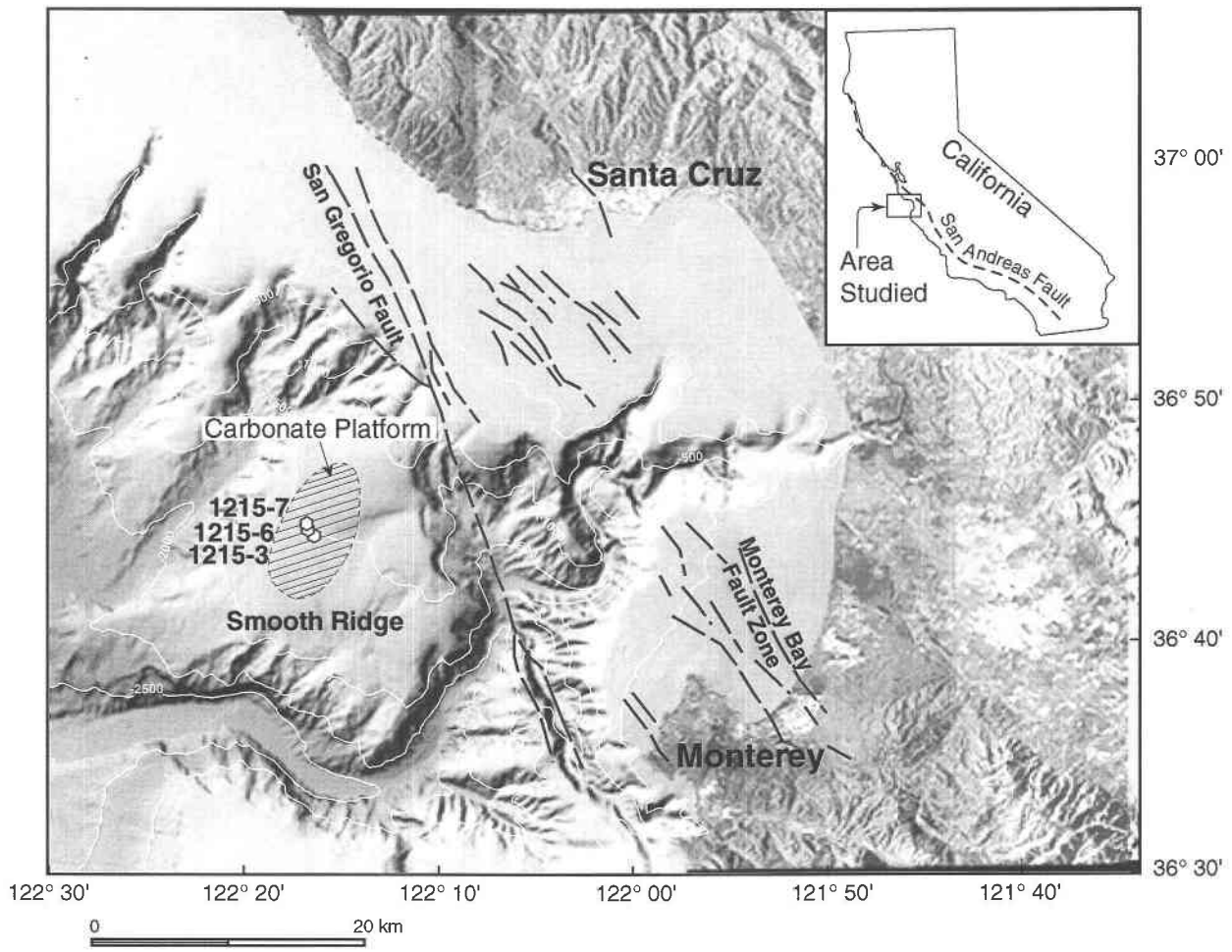

FIGURE 1. Map of Monterey Bay, coastal California, showing location of samples analyzed in this study. Inset shows location of Monterey Bay and its association with the San Andreas fault system. All samples were obtained from sediment push cores collected by the MBARI ROV Ventana.

data highlight the compositional heterogeneity of sedimentary pyrite, as has been also found in previous ion microprobe studies (e.g., Eldridge et al. 1988; McKibben and Eldridge 1989; Riciputi et al. 1996). However, based on textural and chemical arguments, we additionally propose that much of the isotope variability in marine sedimentary pyrites can be explained by a conceptually simple mechanism: heterogeneous colonization of organic material by sulfate-reducing bacteria coupled with systematic temporal variations in sulfur isotope compositions.

GEOLOGICAL AND GEOCHEMICAL SETTING

Expulsion of H_2S and methane-rich fluids at cold seeps provide the dominant chemical and geographic control on the occurrence of pyrite in the sediments of Monterey Bay. On a regional scale, these cold seeps are driven by a combination of tectonic compression, sedimentary loading, diagenesis, and catagenesis; the location of surface seepage is controlled by fault zones sympathetic to the San Andreas system, mud volcanism, and geomorphically focused flow (Orange et al. 1998; Fig. 1). Exact flow rates are too slow to measure directly, but seeps with higher flow rates are characterized by complex chemosynthetic communities that include *Beggiatoa*—a sulfur-oxidizing bacterium—as well as macrofauna such as vesicomyid and solemyid clams and vestimentiferan worms (Barry et al. 1996, 1997; Martin et al. 1997), which are dependent on symbiotic sulfur-oxidizing bacteria (Fisher 1990; Fiala-Médioni et al. 1994). Surrounding regions with lower seep rates have active carbonate precipitation and support extensive mats of *Beggiatoa.*

Chemical and isotopic compositions of the cold-seep fluids are controlled by bacterial processes: carbon isotope compositions of vesicomyid clam tissue (Barry et al. 1996), pore-fluid methane (Martin et al. 1997), and authigenic carbonate (Stakes et al. 1998), as well as hydrogen isotope compositions of methane and high ratios of $C_1/(C_2+C_3)$ (Martin et al. 1997), all indicate that most of the CH_4 is produced by methanogenic bacteria at depth, and that the H_2S is the product of sulfate-reducing bac-

teria. Pore-water chemistry measured by Martin et al. (1997) and Barry et al. (1997) in high-flow areas shows high H_2S concentrations (5–10 m*M*) in the top 10 cm of sediment, and decreases in SO_4 concentrations from seawater values (~30 m*M*) at the sediment-water interface to <5 m*M* at 10–20 cm depth. These observations imply a shallow zone of sulfate reduction. Immediately outside the seeps, SO_4 concentrations are still 15 m*M* at 20 cm depth (Martin et al. 1997) and, elsewhere in coastal California, similar decreases in SO_4 concentrations are observed over sediment thicknesses of 0.5 to 2 m (Kaplan et al. 1963). The upward flow of anoxic fluids within the seeps locally compresses chemical gradients, allowing anaerobic sulfate-reducing bacteria to survive close to the sediment-water interface (Barry et al. 1997; Martin et al. 1997). The presence of these sulfate-reducing bacteria near the top of the sediment and their production of copious H_2S stabilizes higher-level communities of sulfur-oxidizing bacteria and their macrofaunal dependents.

Samples were collected from small sediment ponds exposed near the center of a 300 m diameter zone of anomalous sea floor characterized by carbonate pavements and cold seeps along the axis of "Smooth Ridge," a northeast to southwest trending topographic feature at ~1000 m depth and ~14 km west of the San Gregorio strike-slip fault zone (Fig. 1). Sediments were sampled at a depth of 1000–1007 m using push cores deployed by a remotely operated vehicle (ROV, Ventana), which is maintained by the Monterey Bay Aquarium Research Institute. These samples invariably contain abundant remains of benthic and planktonic foraminifera and, in the deeper push core intervals, 70–80% of the sediment in the >63 μm size range (40% of the total sample) is composed of calcareous microfauna (Salamy 1997). One diagnostic benthic foraminifera, *Uverigerina peregrina,* has been recently observed living in *Beggiatoa* mats on the floor of Monterey Bay (K. Buck, personal communication, 1997).

Pyrite was found both at the sediment surface and within the sediment column, and constitutes an estimated 2–4% of the total sediment >63 μm in size. Grains at the sediment/water interface probably formed there, as the area is actively accumulating sediment. Most grains are compact aggregates of framboids that form pseudomorphs after the 0.1–1 mm diameter chambers of the tests of foraminifera, although some irregularly shaped grains are also present. Casts include species of both benthic and planktonic foraminifera, indicating post-mortem mineralization (Salamy 1997). For clarity, we use the term "grain" to describe both the relatively large textural pseudomorphs and the irregularly shaped grains, and the term "framboid" to describe the 5–10 μm diameter, approximately spherical agglomerations of pyrite microcrystals that comprise most of the grains.

Textures and timing of framboid growth

Textures play a key role in understanding and interpreting the sulfur isotopic compositions measured in our pyrites. Secondary and backscattered-electron (BSE) imaging reveals that the interiors of grains consist of pyrite ± void space; other minerals are rare. Detrital quartz and feldspar are common between chambers, but carbonate is uncommon. X-ray diffraction (XRD) patterns on bulk samples show only well-crystallized pyrite with minor quartz and glauconite. There is no evidence for sulfates or other sulfides such as mackinawite or marcasite. At the sub-micrometer to millimeter scale, BSE images (Fig. 2) show both homogeneous and heterogeneous infilling of foraminiferal test chambers by pyrite. Filling may occur homogeneously from bottom to top leading to non-porous pyrite, or in a "spongiform" or patchy fashion leading to porous material (Fig. 2A). The porous and patchy pyrite is dominated by agglomerated framboids, whereas much of the non-porous pyrite is also framboidal, but contains additional, cementing pyrite (Fig. 2B and 2C). Ordinarily, the cemented framboidal pyrite is overgrown on grain margins by uncemented agglomerated framboids. Interestingly, the interiors of most framboids contain 0.5–1 μm, nearly circular "spots" with a low average atomic number (darker gray) and local void spaces having a similar size (Fig. 2C). These small compositional and textural anomalies may be related to nucleation processes. Finally, a few grains show nearly homogeneous, non-porous pyrite, with isolated indistinct framboids (Fig. 2B). This pyrite typically occurs toward the interiors of large grains (e.g., sample 1215-7) and is overgrown by framboidal pyrite.

These textures represent three different stages in a paragenetic sequence: agglomeration of framboids, cementation, and recrystallization. Thus, porous framboidal pyrite is texturally least mature, and non-porous pyrite with isolated framboids is most mature. Cemented framboidal pyrite represents an intermediate stage; it is clearly older than porous framboidal pyrite, but not yet recrystallized. In later discussion, we use the following terms to describe these different types of pyrite: "RF-pyrite" = non-porous, with relict framboids; "F+I-pyrite" = non-porous, with framboids and interstitial pyrite; and "PF-pyrite" as porous agglomerations of framboids. By this nomenclature, the paragenetic series in the formation of pyrite is then: (1) formation and agglomeration of framboids to produce PF-pyrite; (2) cementation to form F+I-pyrite; and (3) recrystallization to form RF-pyrite.

On average only 5–10 framboids intervene between F+I-pyrite and open pore space or grain margins, whereas typical casts consist of ≥100 framboid diameters. This implies that, although absolute timing cannot be assigned, cementation (formation of F+I-pyrite from former PF-pyrite) is rapid in many grains compared to the total timescale of grain formation. Furthermore, there is no evidence for dissolution of earlier framboids (e.g., truncated margins), suggesting continuous precipitation. The relative temporal sequence, coupled with direct textural observations, shows that growth of authigenic pyrite may be spatially quite complex, and that in completely infilled foraminiferal tests, regions of different age (and hence composition) could occur adjacent to each other. Further-

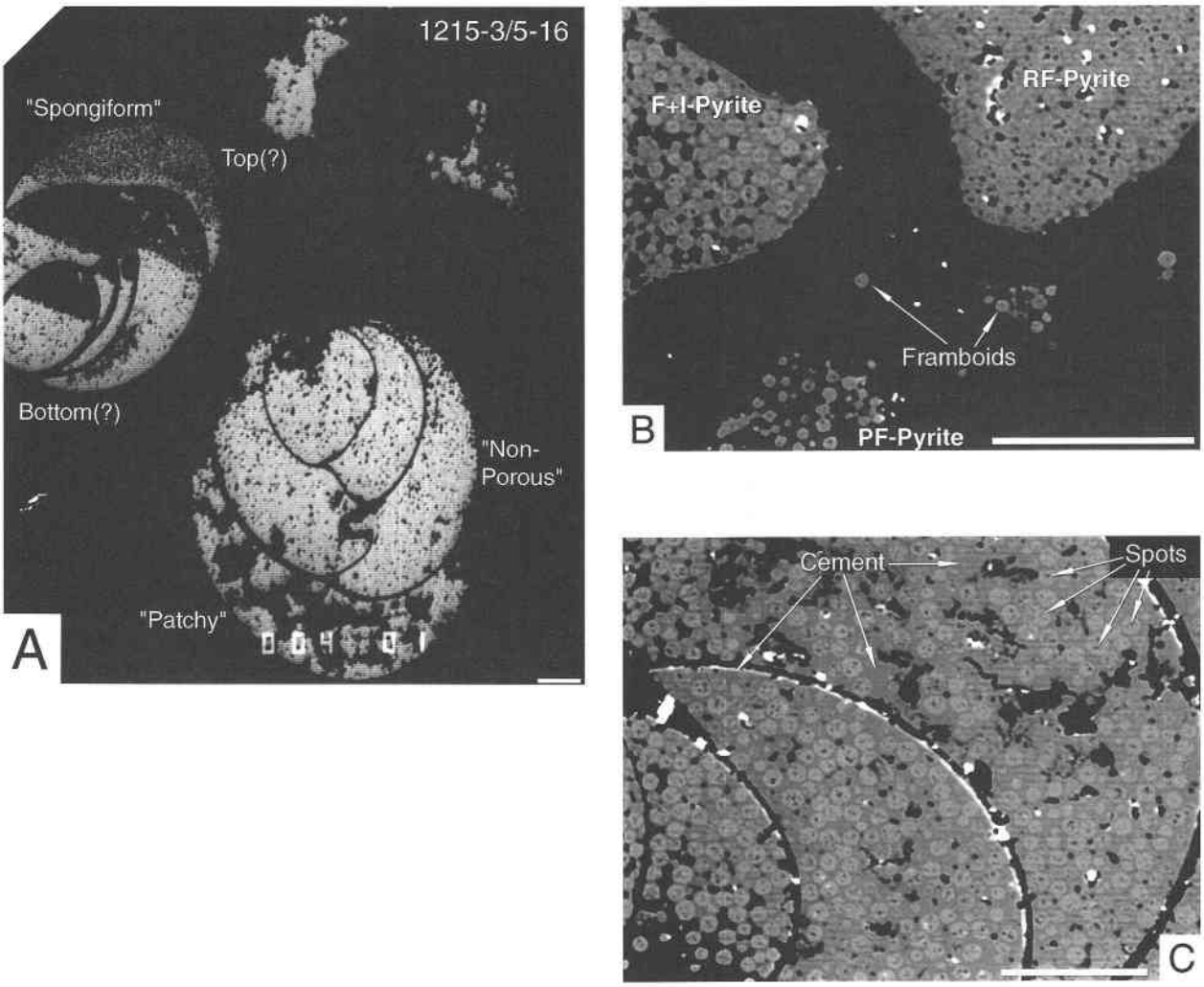

FIGURE 2. BSE images of pyrite grains, illustrating textures that reflect mineral growth processes. Bright areas are pyrite; dark areas are epoxy used for mounting, which originally were open pore space or surrounding sediment. Bright white spots are remnants of the gold-coat. All white scale bars are 100 μm across. (**A**) Sample 1215-3/5-16. Pyrite commonly infills and forms pseudomorphs after foraminiferal tests, but in this sample, infilling has occurred heterogeneously. The upper left test mostly shows a "one-way" (bottom to top?) filling of chambers, but the top chamber also exhibits a unique porous, spongiform texture. In the lower test, infilling of three central chambers by non-porous framboidal and cementing pyrite is nearly complete, but the lowermost chamber retains significant porosity and shows patchy pyrite growth. Numbers along bottom are photographic references for the electron probe. (**B**) Different microscopic pyrite textures developed in 3 adjacent areas of a single grain in sample 1215-7/5-20. Region imaged is shown in Fig. 7. On the margin of the grain (lower part of the image), small, 5–10 μm diameter framboids are loosely connected into a porous aggregate ("PF-pyrite"). On the left, in the tip of the original foram, infilling pyrite consists of clustered framboids with interstitial cementing pyrite, creating a non-porous texture ("F+I-pyrite"); the darker gray of the interstitial pyrite may reflect a greater concentration of intermixed organic matter. On the right, in a different chamber, extensive recrystallization has occurred, obliterating former framboids ("RF-pyrite"). The interiors of grains from other samples (e.g., 1215-7) are similarly non-porous and recrystallized, but occasional framboids are identifiable. (**C**) Interior of grain in sample 1215-7/5-20, illustrating the infilling of chambers by framboids and interstitial pyrite ("F+I-pyrite"). Note that many framboids contain 0.5–1 μm, nearly circular "spots" of low average atomic number (darker gray) and similarly sized void spaces. Region imaged is shown in Fig. 7. The relatively large regions of interstitial pyrite allow comparison of framboid vs. interstitial pyrite chemistry. Compared with framboids, interstitial pyrite compositions show slightly elevated concentrations of Ca, Mg, and Ni, and possibly a lower weight percent total, which may indicate the presence of organic matter.

TABLE 1. Sulfur isotope compositions of biogenic sulfides and the Balmat pyrite standard measured at Lawrence Livermore National Laboratory

Sample	$^{34}S/^{32}S$ (Measured)	Correction	$\delta^{34}S$	$(^{33}S+H)/^{32}S$ (Measured)	Pyrite type
Balmat (6)	0.0401417	1.1375	14.6 ± 0.8	3E-06	
1215-7/0-5a	0.0382883	1.1369	−32.8	4.49E-05	F + I
1215-7/0-5a	0.0384078	1.1363	−30.3	6.28E-05	F + I
1215-7/0-5b	0.0385099	1.1350	−28.8	6.40E-05	RF/F + I
Balmat (2)	0.0402566	1.1343	14.6 ± 0.7	5E-06	
1215-7/0-5a	0.0382416	1.1348	−35.7	6.61E-05	F + I
1215-7/0-5b	0.0386564	1.1353	−24.8	6.34E-05	F + I
1215-7/0-5b	0.0387072	1.1358	−23.1	5.58E-05	F + I
1215-3/5-16a	0.0384489	1.1363	−29.2	8.85E-05	RF
Balmat (1)	0.0401696	1.1367	14.6	7E-06	
Balmat (6)	0.0400933	1.1389	14.6 ± 1.2	8E-06	
1215-7/5-20a	0.0384987	1.1392	−25.5	8.45E-05	F + I
1215-7/5-20a	0.0384285	1.1394	−27.1	8.87E-05	F + I
1215-7/5-20a	0.0386335	1.1397	−21.6	9.16E-05	F + I
1215-7/5-20a	0.0384914	1.1400	−25.0	8.38E-05	F + I
1215-7/5-20a	0.0384690	1.1402	−25.4	8.31E-05	F + I
Balmat (2)	0.0400378	1.1405	14.6 ± 0.8	5E-06	
1215-7/5-20a	0.0384896	1.1402	−24.9	7.69E-05	F + I
1215-7/5-20a	0.0385214	1.1400	−24.2	8.95E-05	F + I
1215-7/5-20a	0.0386163	1.1397	−22.1	8.85E-05	F + I
1215-7/5-20a	0.0386618	1.1394	−21.2	7.60E-05	F + I
1215-7/5-20a	0.0383413	1.1391	−29.6	1.02E-04	F + I
Balmat (2)	0.0400949	1.1388	14.6 ± 0.4	3E-06	
1215-7/5-20a	0.0384565	1.1386	−27.1	6.12E-05	F + I
1215-7/5-20a	0.0387147	1.1383	−20.8	7.33E-05	F + I
1215-7/5-20a	0.0383684	1.1380	−29.8	8.66E-05	F + I
1215-7/5-20a	0.0384868	1.1377	−27.1	5.31E-05	F + I
1215-7/5-20b	0.0382181	1.1374	−34.1	6.21E-05	F + I
Balmat (2)	0.0401558	1.1371	14.6 ± 0.1	3E-06	
1215-7/5-20b	0.0384565	1.1370	−28.4	6.31E-05	F + I
1215-7/5-20b	0.0383841	1.1369	−30.3	6.76E-05	F + I
1215-7/5-20b	0.0383713	1.1368	−30.8	6.67E-05	F + I
1215-7/5-20b	0.0383293	1.1367	−31.9	7.02E-05	F + I
1215-7/5-20b	0.0385105	1.1366	−27.4	6.59E-05	F + I
Balmat (1)	0.0401779	1.1365	14.6	2E-06	
1215-7/5-20b	0.0382640	1.1365	−33.7	9.46E-05	F + I
1215-7/5-20b	0.0384909	1.1366	−27.9	7.29E-05	F + I
1215-7/5-20c	0.0385865	1.1366	−25.5	7.15E-05	F + I
1215-7/5-20c	0.0383299	1.1367	−31.9	8.32E-05	RF
1215-7/5-20c	0.0382013	1.1367	−35.1	7.68E-05	RF
1215-7/5-20c	0.0382199	1.1367	−34.6	8.20E-05	RF
Balmat (1)	0.0401691	1.1367	14.6	3E-06	
1215-4a	0.0380109	1.1371	−39.6	8.19E-05	RF
1215-4a	0.0381911	1.1375	−34.7	7.67E-05	RF
1215-4a	0.0380290	1.1379	−38.5	8.17E-05	RF
1215-4a	0.0382234	1.1383	−33.2	7.35E-05	RF
1215-4a	0.0379670	1.1387	−39.4	8.47E-05	RF
Balmat (1)	0.0400856	1.1391	14.6	12E-06	
1215-3/0-5a	0.0389947	1.1395	−12.7	8.58E-05	F + I
1215-3/0-5a	0.0390078	1.1398	−12.1	8.67E-05	F + I
1215-3/0-5a	0.0386540	1.1401	−20.8	5.68E-05	F + I
1215-3/0-5a	0.0385418	1.1404	−23.4	5.84E-05	F + I
1215-3/0-5a	0.0388383	1.1407	−15.6	6.00E-05	F + I
Balmat (1)	0.0400186	1.1410	14.6	12E-06	
1215-3/0-5a	0.0389087	1.1412	−13.4	7.30E-05	F + I
1215-3/0-5a	0.0392434	1.1414	−4.7	8.17E-05	F + I
1215-3/0-5a	0.0388787	1.1416	−13.8	7.08E-05	F + I
1215-3/0-5a	0.0389731	1.1418	−11.2	7.56E-05	F + I
1215-3/0-5a	0.0389060	1.1420	−12.8	7.04E-05	F + I
Balmat (1)	0.0399757	1.1422	14.6	2E-06	F + I
1215-3/0-5a	0.0389891	1.1418	−10.8	7.57E-05	F + I
1215-3/0-5a	0.0390916	1.1414	−8.6	8.58E-05	F + I
1215-3/0-5b	0.0378083	1.1410	−41.4	7.01E-05	RF/F + I
1215-3/0-5b	0.0379296	1.1406	−38.7	6.52E-05	RF/F + I
1215-7/5-20c	0.0380658	1.1402	−35.6	8.29E-05	RF
Balmat (1)	0.0400636	1.1397	14.6	2E-06	
1215-6/5-15a	0.0380767	1.1404	−35.1	6.57E-05	RF
1215-6/5-15a	0.0381276	1.1411	−33.3	6.08E-05	RF
1215-6/5-15a	0.0387083	1.1417	−18.0	8.79E-05	F + I
1215-6/5-15a	0.0381483	1.1424	−31.6	6.49E-05	RF
1215-6/5-15a	0.0386017	1.1430	−19.6	9.37E-05	F + I
Balmat (1)	0.0400990	1.1436	14.6	2E-06	

TABLE 2. Sulfur isotope compositions of biogenic sulfides and the Balmat pyrite standard measured at Oak Ridge National Laboratory

Sample	$^{34}S/^{32}S$ (Measured)	Correction	$\delta^{34}S$	Pyrite type
Balmat (4)	0.043982	1.0387	15.1 ± 0.3	
1215-6/0-5a	0.042123	1.0387	−27.8	F + I (?)
1215-6/0-5a	0.041821	1.0387	−34.8	?
1215-6/0-5a	0.042034	1.0387	−29.8	?
1215-6/0-5a	0.042003	1.0387	−30.6	F + I (?)
1215-6/0-5b	0.042432	1.0387	−20.6	F + I
1215-6/5-15b	0.041555	1.0387	−40.9	F + I
1215-6/5-15b	0.041849	1.0387	−34.1	F + I
1215-4b	0.041945	1.0387	−31.9	F + I
Balmat (5)	0.043610	1.0475	15.1 ± 0.5	
1215-6/5-15c	0.041923	1.0475	−24.2	F + I
1215-6/5-15c	0.041891	1.0475	−24.9	F + I
1215-6/5-15c	0.041551	1.0475	−32.8	F + I
1215-6/5-15c	0.041555	1.0475	−32.7	RF
1215-6/5-15c	0.041479	1.0475	−34.5	RF
1215-6/5-15c	0.041633	1.0475	−30.9	F + I
1215-6/5-15c	0.041710	1.0475	−29.1	F + I
1215-6/5-15c	0.041442	1.0475	−35.4	RF
1215-6/5-15c	0.041900	1.0475	−24.7	F + I
1215-3/5-16b	0.041325	1.0475	−38.1	F + I

Note: The correction factor obtained for Balmat pyrite (15.1‰, Crowe and Vaughan 1996) at the start of data collection applies to all analyses obtained in that session. The pyrite texture in sample 1215-6/0-5a was difficult to image.

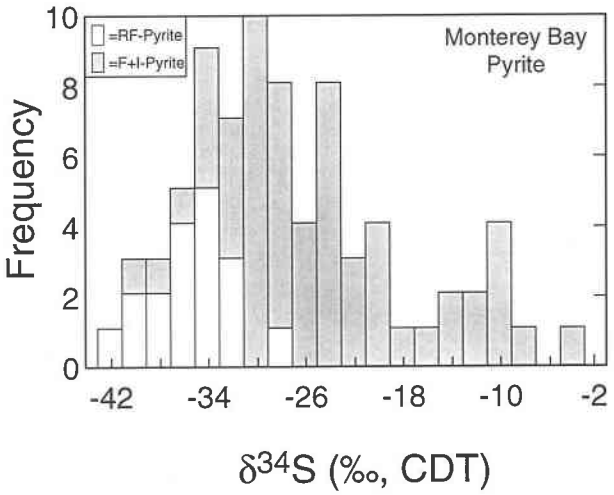

FIGURE 3. Histogram of ion microprobe analyses of sulfur isotope compositions of pyrite grains. White columns are pyrites that appear recrystallized ("RF-pyrite"). Gray columns are pyrites that are either framboidal ("F+I-pyrite") or whose texture is unidentified. The peak of the entire distribution is centered at approximately −30‰, but it is skewed with a long tail to higher $\delta^{34}S$ values. RF-pyrite tends to have the lowest $\delta^{34}S$ values.

more, although the three stages of sulfide formation may provide a useful temporal paradigm for any one grain, because nucleation and growth of pyrite in different foraminiferal tests may be diachronous, there is no direct way to correlate textures and time between different grains.

ANALYTICAL TECHNIQUES

Ion probe analyses

Sulfur isotopes were measured at Lawrence Livermore and Oak Ridge National Laboratories, using Cameca 3f (LLNL) and 4f (ORNL) ion microprobes (Tables 1 and 2). Sulfur isotopic compositions are reported in per mill relative to Cañon Diablo Troilite (CDT), to the nearest 0.1‰ in the tables and to the nearest 0.5‰ (ORNL) and 1‰ (LLNL) in Figures 3, 4, 5, 6, and 7.

An extreme energy filtering method was used at ORNL to measure $^{34}S/^{32}S$ (Riciputi et al. 1996; Paterson et al. 1997). A Cs^+ primary beam with an impact energy of 14.2 KeV was used to sputter through the gold-coat on polished samples and to produce S^- ions. The primary ion beam was defocused to ~20 μm diameter, and a typical beam current of ~0.5-3 nA and an energy offset of 300 ± 20 eV were used. A combination of apertures, slits, and lenses produced a mass resolution of 400. Counts were collected on an electron multiplier with count times of 1 s for ^{32}S and 5 s for ^{34}S, and 70–80 ratios were measured for each spot. At the beginning of each analysis, the primary beam intensity was adjusted to yield the same count rate on ^{32}S to minimize any potential effects from deadtime corrections or non-linearity in the electron multiplier response. These rates were ~1.4×10^6 cps (±5%) for analyses in June 1997, and ~5×10^5 cps for analyses in January 1998. Homogeneous pyrite from the Balmat mine, NY (+15.1‰; Crowe and Vaughan 1996) was used as a working standard to monitor and correct for instrumental mass bias following the procedures of Patterson et al. (1997). The duration of each analysis was typically ~10 min. The internal precision was 0.35–0.5‰ (1 σ) for analyses of 70–80 ratios, essentially identical to the spot-to-spot reproducibility of analyses on the standard (Paterson et al. 1997). Although pyrite is electrically conductive, an electron flood gun was used in the event that inclusions of insulating material were encountered.

Ion microprobe analyses at LLNL were collected with a primary accelerating voltage of 10 KeV, a secondary extraction voltage of 4.5 KeV, a mass resolution of

←

Note: Sampling numbers indicate location, sediment depth, and grain; for example "1215-6/5-15c" indicates the third grain analyzed from sediment between 5 and 15 cm depth from location 1215-6. Numbers in parentheses after Balmat indicate the number of analyses averaged to obtain the correction factor, and ± values show the reproducibility of different analyses collected on the standard at that time. The correction factor for the intervening biogenic sulfide analyses was determined by interpolation between the average measured ratios of Balmat pyrite, its known $\delta^{34}S$ relative to CDT (14.6‰, Crowe et al. 1990), and the sulfur isotope ratio of CDT (0.0450045; Ault and Jensen 1962; this yields $^{34}S/^{32}S = 0.04568$ in Balmat pyrite). Pyrite types are described in the text: F + I = framboidal + interstitial pyrite and RF = pyrite with relict framboids.

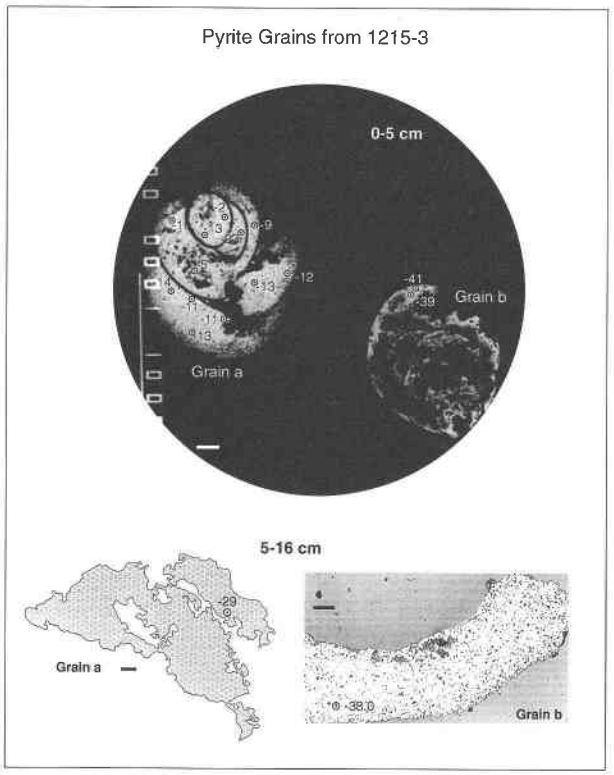

FIGURE 4. Specific sulfur isotope compositions ($\delta^{34}S$) measured in Monterey Bay samples, arranged by sample. Scale bars are all 100 μm. LLNL analyses are rounded to the nearest 1‰, and ORNL analyses to the nearest 0.5‰. BSE image, sketch, and reflected light photomicrograph of pyrite grains from sample 1215-3. In sample 1215-3/0-5 (top image) "Grain a" compositions are quite heterogeneous: relatively high and low $\delta^{34}S$ values occur in the interior, and there is no clear systematic change in composition from one chamber to another. However, the lower $\delta^{34}S$ values occur in non-porous portions of the pyrite, whereas the higher values were found either toward the margin of the grain, or in a patchy portion of the interior. The low $\delta^{34}S$ values in "Grain b" correspond to pyrite texturally intermediate between RF- and F+I. The grains analyzed from sample 1215-3/5-16 (lower two images) are uncommon in that they do not form pseudomorphs after foraminiferal tests.

~2400, an energy window of ±33eV, and no voltage offset. Two of the grain mounts analyzed were coated with carbon and four with gold. The beam was focused to <10 μm as the gold- and carbon-coats were sputtered through and to ≤5 μm during analysis. The response of the electron multiplier at LLNL was found to be affected by the beam intensity of the previously analyzed ion, so that there was some electronic "memory effect" in the ^{34}S counts from the previous ^{32}S signal. To circumvent this problem, ^{32}S was measured on a Faraday cup, leaving ^{34}S on the electron multiplier. The relative counting efficiency of the electron multiplier to the Faraday cup was then determined by comparative analysis of the Balmat pyrite standard, yielding an EM/FC relative response of 0.948. The intensity of the primary ion beam was adjusted at the start of each analysis to yield a count rate on ^{32}S of ~1.15×10^6 (approximately ±5%; count rate for ^{34}S of ~5×10^4), count times were 1 s on ^{32}S and 8 s on ^{34}S, and 15 ratios were measured per spot. In addition, the intensity of the $H^{33}S$ peak was measured for 1 s per cycle to monitor for possible organic and extraneous mineral contamination. Balmat pyrite was also used to monitor instrumental mass fractionation, but its reported isotopic composition (14.6‰; Crowe et al. 1990) is slightly different from the pyrite used at ORNL (15.1‰). Total analysis time was ~15 min, and repeated analysis of the standard yielded an analytical reproducibility of approximately ±1‰ (1 σ).

Because there is no systematic difference in the $\delta^{34}S$ values and hydrogen content of the material analyzed (data in Table 1), we do not believe that the potential occurrence of organic matter biased sulfur isotope measurements. Furthermore, ion probe analysis at ORNL of different metal sulfides and fine-grained materials shows that the small differences in trace metal concentrations in framboidal vs. interstitial pyrite or small amounts of sulfur-free contaminants could not have caused significant differences in instrumental mass fractionation, which might lead to spurious analyses.

Electron probe analyses

Chemical compositions of framboids and interstitial cements in F+I-pyrite (Table 3) were determined using the fully automated JEOL 733 electron microprobe at LLNL. Operating conditions included an accelerating voltage of 15 KeV; a flag current on brass of 250 nA; four wavelength dispersive spectrometers; and natural and synthetic pyrite, silicates, and metals as standards. Elements analyzed included S, Fe, O, Mg, Ca, Mn, Co, Ni, Cu, Zn, As, and Pb, with count times of 10 s for S and Fe, 25–30 s for O, and 120 s for all other elements. For the trace and minor elements, these conditions resulted in minimum detection limits of 50–100 ppm, excepting Mg and O (~25 ppm), and Ni (1500 ppm).

RESULTS

Sulfur isotopes

Pyrite is generally depleted in ^{34}S, with $\delta^{34}S$ values ranging from −41 to −5‰ (Tables 1 and 2, Figs. 3, 4, 5, 6, and 7). The distribution is skewed with most values in the range −35 to −25‰, and a tail toward higher $\delta^{34}S$ (Fig. 3). There is no correlation between $\delta^{34}S$ and sample depth. Indeed, the total sulfur isotope variation observed in grains from the top 0–5 cm (1215-3 = −41 to −5‰; 1215-6 = −35 to −20‰; 1215-7 = −36 to −23‰), is quite similar to that obtained from the next 10–15 cm interval (1215-3 = −37 to −29‰; 1215-6 = −41 to −18‰; 1215-7 = −36 to −21‰). The few $\delta^{34}S$ values of pyrite collected at the sediment-water interface (sample 1215-4) are all more negative than −32‰.

Within and among grains from the same sample, variations in $\delta^{34}S$ are both regular and irregular. In several grains (e.g., 1215-4a, 1215-6/0-5a, 1215-6/5-15a, 1215-

TABLE 3. Electron microprobe analyses of framboidal and cementing pyrite

Sample	S	Fe	O	Mg	Ca	Co	Ni	Cu	Zn	Wt% total	$\delta^{34}S$
1215-7/5-20b fram.	52.12	46.24	NA	150	50	550	300	200	ND	98.46	−30
1215-7/5-20b cem.	52.08	44.87	NA	300	400	500	3050	150	ND	97.38	−30
1215-7/5-20b fram.	52.36	46.19	ND	NA	150	500	400	100	ND	98.66	−34
1215-7/5-20b fram.	51.98	46.32	ND	NA	200	450	ND	150	ND	98.38	−27
1215-7/5-20b fram.	52.69	46.13	ND	NA	ND	550	ND	150	100	98.91	−34
1215-7/5-20c fram.	52.58	45.84	1950	NA	200	500	7200	100	ND	99.41	−25
1215-7/5-20c fram.	52.32	45.42	ND	NA	300	450	7300	100	ND	98.56	−36
1215-7/5-20c fram.	51.53	45.22	1950	NA	300	500	4400	50	ND	97.47	−35
1215-7/5-20a fram.	51.83	45.42	850	NA	200	500	6950	150	ND	98.12	−24
1215-7/5-20a fram.	50.71	45.49	1300	NA	300	550	2300	550	ND	96.70	−21
1215-6/5-15a fram.	49.56	43.78	700	NA	250	600	8050	450	250	94.99	−32
1215-6/5-15a fram.	51.50	45.30	650	NA	300	500	6550	200	ND	97.61	−20
1215-6/5-15a fram.	51.85	45.42	2600	NA	200	600	9300	150	ND	98.55	−18
1215-3/0-5b fram.	52.91	45.45	ND	NA	450	550	11250	150	ND	99.60	−41
1215-3/0-5a fram.	52.55	45.01	900	NA	350	450	6300	100	ND	98.36	−23
1215-3/0-5a fram.	47.99	42.60	30900	NA	250	450	13650	100	ND	95.13	−21
1215-3/0-5a fram.	52.18	44.69	6800	NA	300	450	3950	200	ND	98.04	−5
1215-3/0-5a fram.	52.18	45.34	ND	NA	250	500	3600	200	ND	97.97	−13

Note: S and Fe are in wt% to the nearest 0.01. Concentrations of the other elements are in ppm to the nearest 50 ppm. Concentrations of As, Pb, and Mn in sample 1215-7/5-20b were below detection. NA means the element was not analyzed; ND means the element was measured, but was below detection. Four analyses were averaged for the first analysis, and three analyses were averaged for the second. Detection limits were 50–100 ppm, excepting Mg and O (~25 ppm) and Ni (1500 ppm).

6/5-15c, 1215-7/5-20c) $\delta^{34}S$ variations are consistent with systematic increases from one chamber to another, and from the interior of a grain to its exterior (Figs. 5, 6, and 7). In sample 1215-6/5-15a (Fig. 6), the regular increase in $\delta^{34}S$ from core to rim correlates with a progressive change from RF-pyrite in the center of the grain, to F+I-pyrite at the margin. A pseudomorphous grain from the same sample (1215-6/5-15c; Fig. 6) also shows an increase in $\delta^{34}S$ from the central to the outer chambers. The ranges in $\delta^{34}S$ are similar in both grains (−35 to −18‰ in 1215-6/5-15a and −35 to −24‰ in 1215-6/5-15c).

In contrast to the regular zonation and similar compositions exhibited by grains in some samples, other grains show strong intergranular differences in $\delta^{34}S$ values and irregular intragranular zoning. The two grains analyzed in sample 1215-3/0-5 (Fig. 4) show large isotopic differences of 15 to 35‰, and internal isotopic variations in one grain reach nearly 20‰. The isotopically heterogeneous grain (1215-3/0-5a) has relatively high $\delta^{34}S$ values, both on the grain margin and in the patchy pyrite in the interior (all F+I-pyrite). Sample 1215-7/5-20 (Fig. 7), contains grains with quite different isotopic patterns.

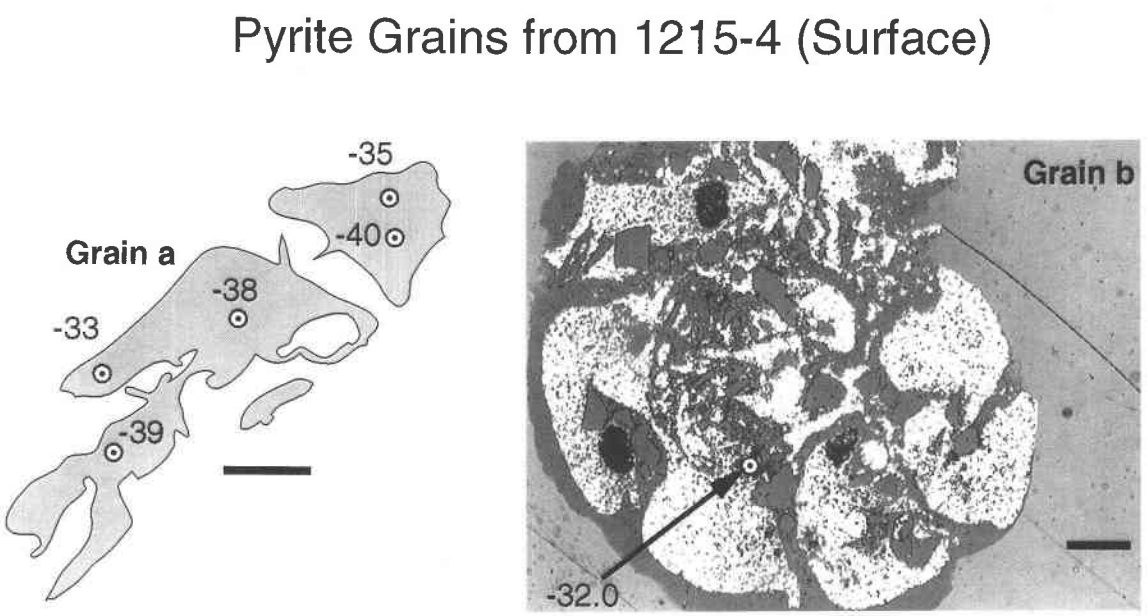

FIGURE 5. Sketch and reflected light photomicrograph of 2 grains from surface sample 1215-4. The grain on the left may have regular zonation, with a low ^{34}S interior and a higher ^{34}S margin. Values for $\delta^{34}S$ in both grains are low compared with many other samples. The ~50 μm diameter, blocky dark gray grains inside "Grain b" are detrital quartz and feldspar.

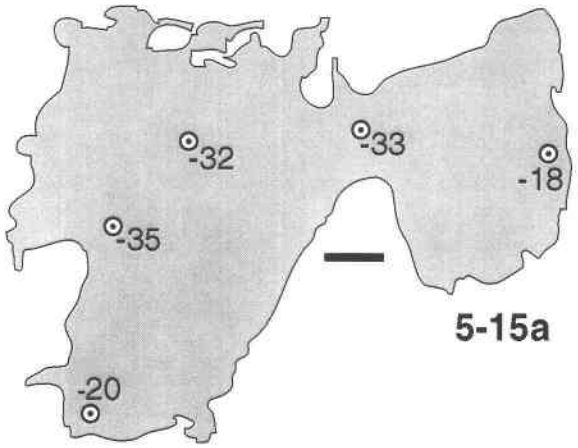
-32
-33
-18
-35
-20
5-15a

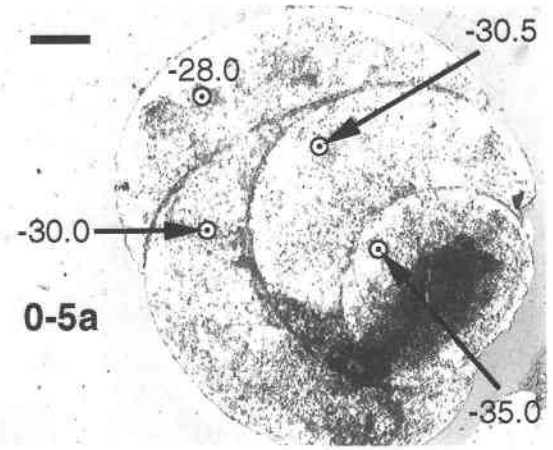
-30.5
-28.0
-30.0
-35.0
0-5a

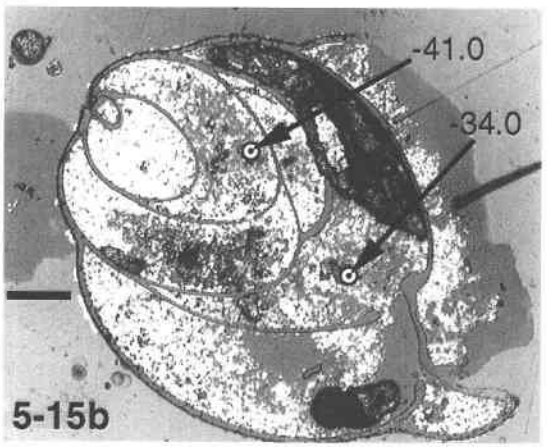
-41.0
-34.0
5-15b

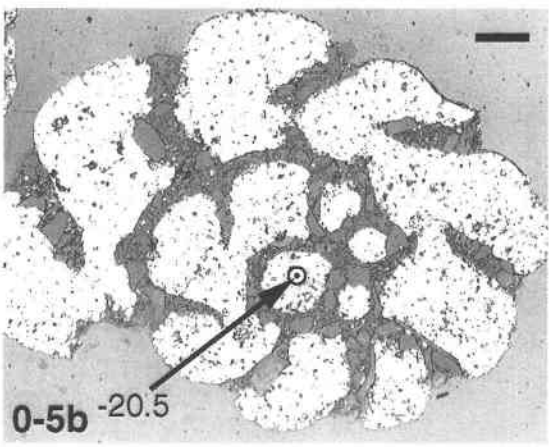
-20.5
0-5b

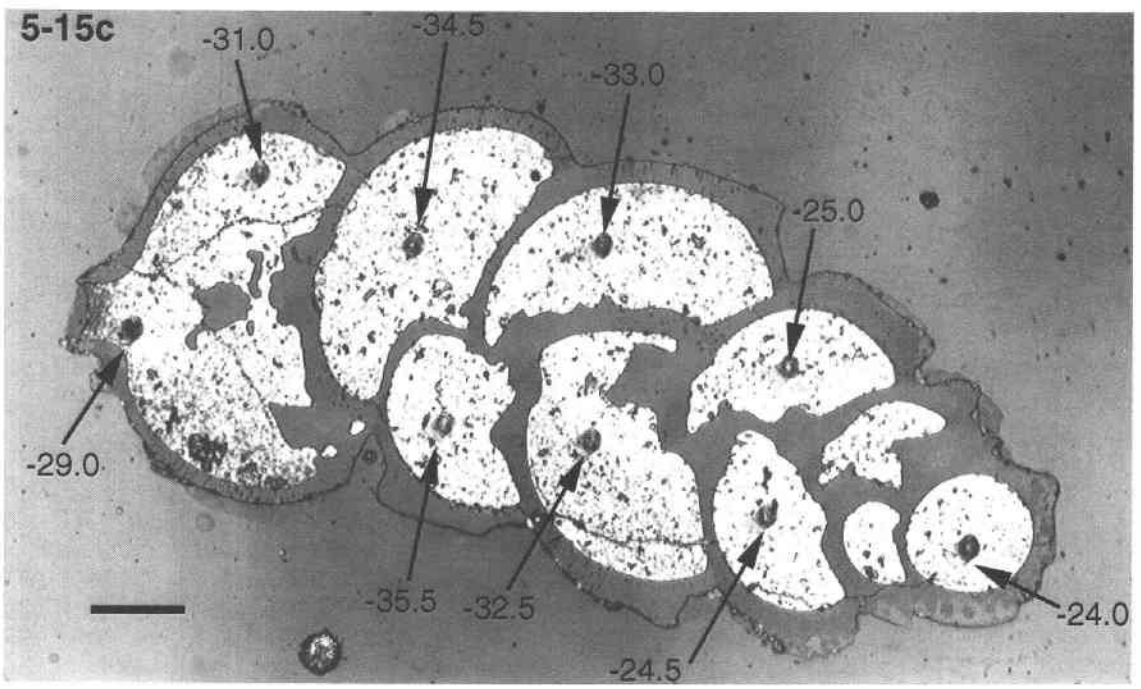
5-15c
-31.0
-34.5
-33.0
-25.0
-29.0
-35.5
-32.5
-24.5
-24.0

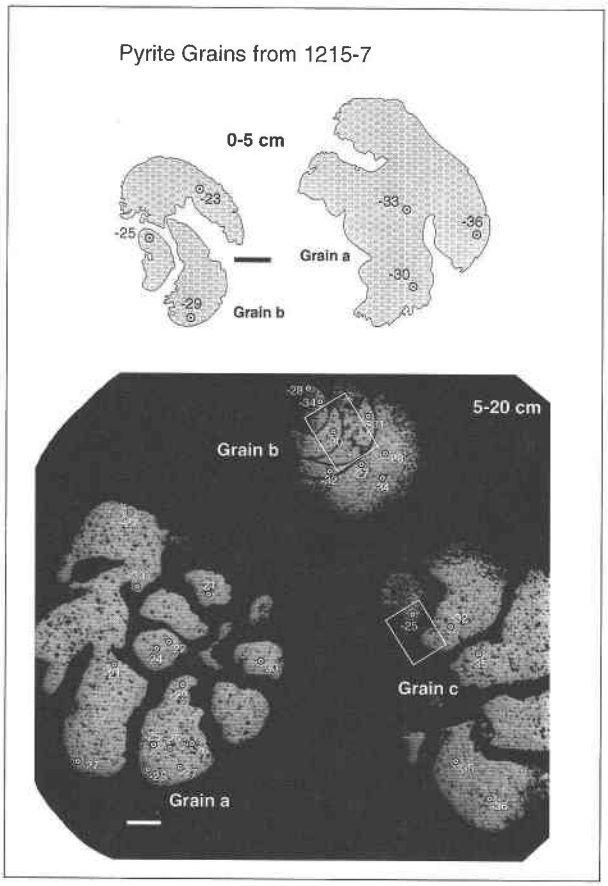

FIGURE 7. In sample 1215-7/5-20, "Grain c" (lower right) shows a systematic increase in $\delta^{34}S$ from the lower chambers (−36 to −32‰, RF-pyrite) to the upper infilled chamber (−25‰, F+I pyrite). However, the other 2 grains are less systematic compositionally, and exhibit isolated high and low $\delta^{34}S$ values. Rectangles on grains "b" and "c" show areas imaged in Figs. 2B and 2C.

Sample 1215-7/5-20a has a central zone with $\delta^{34}S$ values of −21 to −24‰ and an outer margin with $\delta^{34}S$ values of −25 to −30‰. Sample 1215-7/5-20b shows irregular zoning with relatively high and low $\delta^{34}S$ values in the same chamber and heterogeneously distributed between the core and rim of the entire grain. Sample 1215-7/5-20c shows low $\delta^{34}S$ values (−36 to −32‰) in RF-pyrite in most chambers and higher $\delta^{34}S$ (−25‰) in F+I-pyrite of one end chamber. Compositional differences between grains reach 15‰.

Despite the isotopic complexity exhibited by many grains, compositions correlate broadly with texture. In sample 1215-3/0-5 (Fig. 4), the highest $\delta^{34}S$ values occur in F+I pyrite, either toward grain margins or in porous areas. The lowest $\delta^{34}S$ values, although found at the edge of a different grain, are from pyrite that has textural characteristics of both RF- and F+I-pyrite. That is, there may be a general tendency for high $\delta^{34}S$ values to occur in F+I pyrite either near grain margins or porous areas, and for low $\delta^{34}S$ values to occur in recrystallized RF-pyrite in grain interiors. This trend is observed directly in sample1215-6/5-15a (Fig. 6). The compositions measured may be attributable to a temporal increase in $\delta^{34}S$ with time, coupled with nucleation and growth of pyrite that is regular in some grains and heterogeneous in others.

Trace elements

The contrast in BSE intensities for framboidal vs. cementing pyrite in F+I-pyrite (Fig. 2B and C) implies compositional or mineralogical differences, but no clear cause is evident. Reflected light microscopy using crossed polarizers reveals no differences between framboids and interstitial sulfide, indicating that pyrite is the only likely sulfide present. XRD scans also show pyrite as the only sulfide. Trace element analyses (Table 3) suggest that the abundance of elements with $Z \geq 8$ (oxygen) are not sufficiently variable to explain this contrast in BSE intensity. The only measurable compositional differences between interstitial pyrite cement and framboids are a small increase in Mg and Ca concentrations, coupled with a larger increase in Ni (first 2 analyses, Table 3). This contrasts with the results of Saunders et al. (1997) who found large variations in As, Co, Ni, and other trace metals. Although the sporadic variations in O concentrations in our samples may reflect mixtures with interstitial minerals, Ca concentrations are not correlated with O, suggesting no mixing with interstitial carbonates and sulfates. For the beam current used for imaging (~70 nA), concentration changes at the ≤1000 ppm level would not be observed with BSE. One explanation is that interstitial organic matter in the cementing pyrite is responsible for a lower BSE intensity. Organic matter is not resolvable compositionally with the electron probe, because the samples are carbon coated and the other most abundant element, H, cannot be analyzed. However, organics would have a low average atomic number (Z), diminishing the intensity of BSE. Alternatively, some difference in either the crystallinity or crystallite packing in the interstial sulfide might cause a lower BSE intensity.

←

FIGURE 6. Pyrite grains from sample 1215-6 show more regular zonation. In "Grain a" from 1215-6/5-15 (top left), a low ^{34}S core of RF-pyrite (−32 to −35‰) is overgrown by a higher ^{34}S rim of F+I pyrite (−18 to −20‰); in "Grain c" (bottom), there is a systematic change in $\delta^{34}S$ from low values in the central chambers (−32.5 to −35.5‰) to higher values in the end chambers (−24 and −29‰). In sample 1215-6/0-5 cm, "Grain a" (top right) shows a systematic change in $\delta^{34}S$ values from one side of the grain to the other (−35 to −28‰). Note that the compositional range observed in grains from the top 5 cm of sediment (−35 to −20.5‰) is similar to that in grains from the 5–15 cm interval (−35.5 to −18‰).

Discussion

Biotic vs. abiotic origin of framboidal pyrite

Framboidal pyrite (FeS_2) commonly precipitates in association with bacteria but the role, if any, of bacteria in the physical precipitation process remains in dispute. Purely biotic mechanisms were proposed first (e.g., Schneiderhöhn 1923; Love 1957), citing the possible morphological similarity of the aggregates to bacterial colonies. An abiotic mechanism was defended based on the occurrence of framboidal pyrite in high-T hydrothermal veins where bacteria were presumed unlikely to survive (e.g., Steineke 1963), and this mechanism is now largely accepted because of the success in reproducing framboidal morphologies abiotically in the laboratory (e.g., Berner 1969; Farrand 1970; Sweeney and Kaplan 1973; Graham and Ohmoto 1994; Wilkin and Barnes 1996; Rickard 1997). Laboratory studies demonstrate the importance of initial formation of precursor $Fe_{1+x}S_{1-y}$ materials (gels and mackinawite) that transform first to greigite (Fe_3S_4) and then to pyrite (e.g., Sweeney and Kaplan 1973; Schoonen and Barnes 1991b; Wilkin and Barnes 1996; Rickard 1997). Direct formation of pyrite, while thermodynamically favored (Berner 1967), is quite unfavorable kinetically (Schoonen and Barnes 1991a). Indeed, Wilkin and Barnes (1997) argue that common pyrite framboids found in sediments may form by the spontaneous aggregation of colloidal suspensions of greigite, with the aggregation itself being driven by the ferrimagnetism of greigite (single-domain) at particle sizes of 0.1–1 μm.

Although the feasibility of abiotic precipitation of Fe-sulfides is well documented, several factors highlight the importance of bacteria in the sulfide precipitation process, at least in marine settings:

(1) Precipitation of Fe-sulfides requires high H_2S concentrations, and in marine sediments the rapid increase in H_2S concentration with depth is the direct result of the reduction of sulfate by bacteria (e.g., see review of Nealson and Stahl 1997).

(2) Sedimentary framboidal pyrites have a much lower $\delta^{34}S$ than expected if the entire chemical process were abiotic. Abiotic chemical reduction of sulfate to H_2S fractionates sulfur by 12–22‰ (Harrison and Thode 1957; T.H. Donnelly and C.J. Downes, personal communication, cited in Chambers and Trudinger 1979), and the fractionation between H_2S and FeS_2 is ≤1‰ (Chambers and Trudinger 1979; Price and Shieh 1979; Wilkin and Barnes 1996); these fractionations lead to an expected abiotic $\Delta^{34}S(SO_4^{2-} - FeS_2)$ of ~10–25‰. However, the measured fractionation between pore-water sulfate and coexisting sedimentary pyrite is 40–60‰ (e.g., see summary of Chambers and Trudinger 1979). This stronger depletion in pyrite ^{34}S cannot be attributed simply to abiotic mechanisms. The most reasonable explanation for this discrepancy is that microorganisms strongly prefer light isotopes, so that biogenic products (HS^-) have low $\delta^{34}S$ values. Sulfur isotope exchange rates are negligible for SO_4^{2-} and pyrite, whereas they are fast among HS^-, amorphous Fe-sulfides, mackinawite, and greigite (Fossing and Jørgensen 1990; Fossing et al. 1992). The negligible exchange rate and small fractionation for pyrite compared to any likely precursor sulfide imply that pyrite should retain an isotopic composition essentially equal to that of dissolved HS^-. The low $\delta^{34}S$ of pyrite therefore implies a low $\delta^{34}S$ value for pore-water HS^-, which is most plausibly linked to bacterial sulfate reduction.

(3) In Monterey Bay, framboidal sulfides are most commonly found as pseudomorphs after tests of foraminifera, rather than distributed within the sediments. This spatial association with a former C-source may link sulfide precipitation to microbial degradation of organic matter.

(4) Many sulfate-reducing bacteria produce intracellular ferrimagnetic greigite (see review of Bazylinski and Moskowitz 1997). Although as yet unstudied, upon cell death, this greigite could contribute to the formation of framboids.

(5) As summarized by Fortin et al. (1997), metal ions are much more reactive to dissolved sulfide when adsorbed onto cell walls than in solution (Mohagheghi et al. 1985), and bacterial cell walls are a preferred nucleation site for metal sulfide (e.g., Degens and Ittekkot 1982; Ferris et al. 1987). Thus, sulfate-reducing bacteria likely facilitate the formation of microcrystals, which may then form framboids.

Although it may be impossible to demonstrate unambiguously that bacteria benefit from and hence directly control the precipitation of extracellular sulfides, there are conclusive links between bacterial activity and the occurrence of Fe-sulfides, and between the sulfur isotope compositions of framboidal pyrite and the products of bacterial sulfate reduction. Although precipitation is perhaps rarely biologically "controlled," it is unquestionably biologically "induced" (terminology of Bazylinski and Moskowitz 1997, after Lowenstam 1981) both chemically and possibly physico-kinetically.

Isotopic compositions

The low measured $\delta^{34}S$ values for Monterey Bay pyrite (−41 to −5‰) are generally consistent with mediation of pore-water and sulfide mineral chemistry by sulfate-reducing bacteria. The likely source of sulfate from which the pyrite was precipitated is modern sea water, which has a sulfur isotope composition of approximately +20‰ (Kaplan et al. 1963; Rees et al. 1978). If the lowest $\delta^{34}S$ values (approximately −40‰) formed earliest in equilibrium with isotopically unaltered sea water sulfate, then $\Delta^{34}S(SO_4^{2-} - \text{sulfide})$ is ~60‰. As described above, it is unlikely that these compositions reflect abiotic precipitation. However, it also not clear how biotic mediation causes sulfate-sulfide fractionations of ~60‰. Laboratory studies with sulfate-reducing bacteria show a maximum sulfate-sulfide fractionation of ~40‰, yielding pyrite of approximately −20‰ (Chambers and Trudinger 1979; Canfield and Thamdrup 1994; Canfield and Teske 1996; Habicht and Canfield 1997; Lyons 1997). This

maximum fractionation may explain some measured $\delta^{34}S$ values, but is still 10–20‰ smaller than needed to explain nearly half of our data (Fig. 3). This problematic discrepancy is common, in that diagenetic pyrite from modern marine sediments in many cases has an isotopic composition of −20 to −40‰ (Chambers and Trudinger 1979; Canfield and Teske 1996).

Several explanations have been proposed for the difference between laboratory and natural isotopic fractionations. One possibility is that isotopic exchange occurs between different sulfur sources after precipitation of sulfides (Chambers and Trudinger 1979), but this is unlikely because the isotopic exchange rate of pyrite is extremely slow (Fossing and Jørgensen 1990; Fossing et al. 1992). A common alternative explanation notes the broad correlation between increased $\Delta^{34}S(SO_4^{2-}$ − sulfide) and decreased sulfate-reduction rate (e.g., Fig. 5 of Chambers and Trudinger 1979). Natural sulfate reduction rates may be several orders of magnitude slower in nature than in the laboratory (Goldhaber and Kaplan 1980; Skyring 1987), implying larger natural fractionations than observed experimentally. An intriguing third theory (Canfield and Thamdrup 1994) emphasizes the role of sulfur-disproportionating bacteria. These bacteria disproportionate elemental sulfur, formed by H_2S-oxidizing bacteria, into high ^{34}S sulfate and low ^{34}S sulfide. Loss of sulfate from the system then causes a progressive ^{34}S depletion in residual dissolved and precipitated sulfide. Repeated cycling of sulfide oxidation followed by sulfur disproportionation could potentially lead to larger sulfur isotope fractionations than are observed in the laboratory. Verification of this process in nature would further emphasize the key role that bacteria, acting individually and in concert with other microorganisms, can play in controlling stable isotopes and chemistry in marine sediments.

The observed increase in $\delta^{34}S$ from core to rim in some sulfide grains (e.g., 1215-6/5-15a) is consistent with Rayleigh fractionation in a closed system during sulfate reduction. In this process, low ^{34}S HS^- forms by reduction of sulfate, and is either sequestered in grain interiors as sulfide or escapes diffusionally through the overlying sediment. This preferential loss of low ^{34}S material causes an increase in the ^{34}S of residual pore-fluid sulfate and hence of later reduced HS^- and resulting precipitated sulfides. Thus, the $\delta^{34}S$ value of a pyrite grain increases both with time and with depth as new sulfidic material with an increasingly high ^{34}S content is added during burial. Such a process is well-documented in fine-grained marine sediments, in which the $\delta^{34}S$ values of both pore-water sulfate and either soluble or authigenic sulfide increase with depth, as pore-water sulfate concentrations decrease (e.g., Kaplan et al. 1963; von Hartmann and Nielsen 1969; Goldhaber and Kaplan 1980; Canfield et al. 1992). Because of this well-characterized chemical and isotopic trend, it is not surprising that the $\delta^{34}S$ values of some of our sulfides apparently increased with time.

Assuming a Rayleigh distillilation process, it is possible to calculate the amount of sulfate removed from pore waters. For an estimated sulfate-sulfide fractionation of 60‰, a shift from −40‰ to −5‰ would require removal of ~50% of the sulfate. Most compositions are not so shifted, and a shift in $\delta^{34}S$ values from −40 to −20‰ requires removal of only 30% sulfate. The interval within the sediment over which this process occurs in Monterey Bay sediments is quite uncertain. Chemical analysis of pore fluid chemistry in the active seeps (Barry et al. 1997; Martin et al. 1997) indicates that the sulfide precipitation zone may be as compressed as 10 cm, with sulfate concentrations dropping by a factor of two in the top 5–10 cm. Because grains from the upper 5 cm are texturally and compositionally indistinguishable from grains collected from deeper sediment, formation of most sulfide grains may well be complete after burial to 5 cm.

Role of bacteria

Most difficult to interpret is the strong isotopic heterogeneity exhibited among grains in the same samples and within individual grains. We propose that the isotopic differences among otherwise similar grains and the irregular zoning within grains may well reflect heterogeneous colonization and growth by bacteria inside foraminiferal tests. Such a mechanism is supported by the following observations: (1) the interior of the tests provides a ready C-source and open space for bacterial growth; (2) sulfur isotope compositions are clearly linked to bacterial processes; (3) growth of bacterial colonies is likely to be heterogeneous as they expand on old substrates as well as colonize newly available regions; and (4) bacterial cell walls may act as nucleation sites for sulfides, so that wherever bacteria grow, sulfides are likely to form.

In support of point 4, Sweeney and Kaplan (1973) found that formation of sulfide framboids was enhanced when spherical nuclei were available, and Ferris et al. (1987) showed that bacterial cell walls also enhance sulfide precipitation. Furthermore, Kaplan et al. (1963) suggested that chemical micro-environments play an important role in sulfide precipitation, so that sulfides are expected to form in close association with bacteria. One interpretation of the 0.5–1 μm approximately circular, low-Z spots and void spaces (Fig. 3C) is that these are the remnants of bacteria that helped initiate framboid formation. For example, scanning electron microscope images presented by Blake et al. (this volume) show that, during their experiments, bacteria were trapped in balls of precipitating apatite. Perhaps bacteria can be similarly entrapped during precipitation of sulfides.

Several alternative interpretations of the isotopic heterogeneity are possible, and most generally require combined regular and irregular changes in pore-fluid ^{34}S in time and space so that the compositions and crystallization kinetics of pyrite are decoupled from any systematic process. For example, erratic variations in pore fluid discharge rates and compositions could alter chemical gradients and isotopic compositions, dissolving pyrite at some times and reprecipitating new pyrite of a different $\delta^{34}S$ value at others. This hypothesis is not favored by

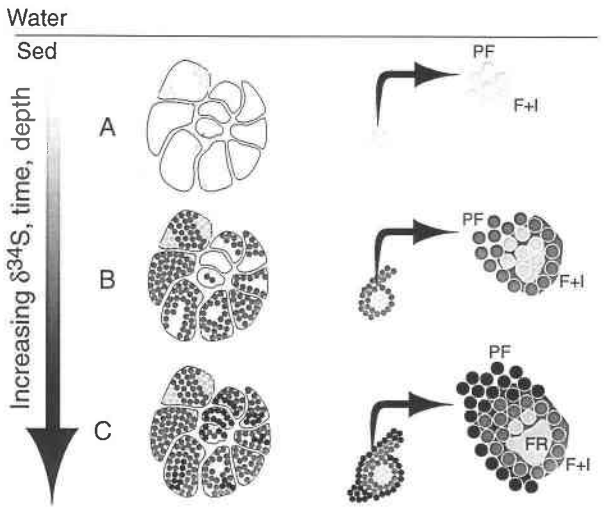

Figure 8. Cartoon of how heterogeneous bacterial colonization of foraminiferal tests coupled with Rayleigh fractionation of sulfur isotopes in a closed system can lead to sulfur isotope heterogeneity within and among sulfide grains. Dots represent framboids, and darker grays represent high $\delta^{34}S$. (A) Initial nucleation and growth of low $\delta^{34}S$ framboids high in the sediment column (light gray dots) is rapidly succeeded by cementation (light gray interstitial material). (B) With increased burial, new framboids form with higher $\delta^{34}S$ values and aggregate in new regions or on old substrates. (C) In the most mature samples, recrystallization of early formed F+I-pyrite forms RF-pyrite (light patch), as additional framboids form and cement (black). Compositional zoning may be extremely heterogeneous (left) or grossly concentric (right).

present observations, since chemical gradients in the uppermost sediments did not change in six months at a few specific Monterey Bay sites (Martin et al. 1997) and dissolution features are not obvious in any of the sulfide grains we studied. However, the time scale of pyrite formation is not known, and evidence for dissolution may be subtle compositionally and texturally. We cannot rule out any process, biotic or abiotic, that might allow such heterogeneous growth of pyrite. Nonetheless, we believe that chemical and textural evidence favor a fundamental bacterial control on the precipitation of sulfide in our samples: Variations in bacterial colonization provide a conceptually simple and potentially testable mechanism for producing all the observed compositional and textural variations.

If our proposal is correct, then bacterial growth processes may possibly be tracked using sulfide textures and compositions (Fig. 8). Initial colonization by sulfate-reducing bacteria causes formation and agglomeration of framboids to produce early PF-pyrite (light dots). High concentrations of dissolved sulfide in the fluid cause cementation of the framboids soon after they are formed (F+I-pyrite), thereby displacing the bacterial colony. With continued growth of the colony and burial in the sediment, framboids and cement continue to form with higher $\delta^{34}S$ values (darker gray, Fig. 8). At the deepest level (several centimeters?), framboid formation and cementation continues (black dots and regions, Fig. 8), and the earliest-formed pyrite recrystallizes to RF-pyrite (light patch). Thus, the different textures and compositions of sulfides (low-$\delta^{34}S$ RF, intermediate-$\delta^{34}S$ F+I, and high-$\delta^{34}S$ PF) may in favorable cases be used to infer growth of bacteria. Clearly, the complexity of sulfide nucleation and growth processes in sediments warrants additional research into the biotic and abiotic factors that control sulfur isotope signatures.

Finally, we note that bulk analyses of our pyrite grains would not likely have resolved the changes in sulfur isotope compositions revealed by the ion probe. Grains from different sediment levels show similar isotopic ranges and patterns, and had whole grains or multiple grains been analyzed in bulk, the strong internal heterogeneity would have been missed. Because some studies have revealed strong changes in bulk pyrite $\delta^{34}S$ values with depth, our results suggest that even more extreme isotope changes may occur than has been previously recognized.

Acknowledgments

We thank D. Phinney and I. Hutcheon for their expertise with the LLNL on probe, T. Kakegawa, J. Saunders, and J. Banfield for their reviews and comments, D. Crowe and J.W. Valley for providing the Balmat pyrite standards, and K. Salamy for drafting most of Figure 1 and for separating the pyrite grains analyzed in this study. M.J.K.'s research was supported by IGPP-Livermore and a grant from the DOE's Office of Basic Energy Sciences (to F.J. Ryerson) at LLNL under the auspices of contract W-7405-Eng-48. L.R.R.'s research was sponsored by the Geosciences Program, Office of Basic Energy Science, Department of Energy, under contract DE-AC05-96OR 22464 with Oak Ridge National Laboratory, managed by Lockheed Martin Energy Research Corporation. D.S. thanks the captain and the crew of the ROV Pt. Lobos, the pilots of the ROV Ventana for enthusiastic assistance during the collection of these samples, and K. Buck for discussing associations between bacteria and foraminifera. The field operations and effort of D.S. were supported by the Lucille and David Packard Foundation. D.L.O.'s early work on cold seeps in Monterey Bay was supported by MBARI, and his current study of seepage is supported by ONR grants N00014-93-1-0202 and N00014-96-1-0361.

References cited

Ault, W.V. and Jensen, M.L. (1962) Summary of sulfur isotope standards. In M.L. Jensen, (Ed.), Biogeochemistry of Sulfur Isotopes. Yale University, New Haven, Connecticut.

Barry, J.P., Greene, H.G., Orange, D.L., Baxter, C.H., Robison, B.H., Kochevar, R.E., Hybakken, J.W., Reed, D.L., and McHugh, C.M. (1996) Biologic and geologic characteristics of cold seeps in Monterey Bay, California. Deep-Sea Research, 43, 1739–1762.

Barry, J.P., Kochevar, R.E., and Baxter, C.H. (1997) The influence of porewater chemistry and physiology on the distribution of vesicomyid clams at cold seeps in Monterey Bay: implications for patterns of chemosynthetic community organization. Limnology and Oceanography, 42, 318–328.

Bazylinski, D.A. and Moskowitz, B.M. (1997) Microbial biomineralization of magnetic iron minerals: microbiology, magnetism and environmental significance. Mineralogical Society of America Reviews in Mineralogy, 35, 181–223.

Berner, R.A. (1967). The thermodynamic stability of sedimentary iron sulfides. American Journal of Science, 265, 773–785.

———(1969). The synthesis of framboidal pyrite. Economic Geology, 64, 383–384.

———(1970). Sedimentary pyrite formation. American Journal of Science, 168, 1–23.

———(1984). Sedimentary pyrite formation: An update. Geochimica et Cosmochimica Acta, 48, 605–615.

Blake, R.E., O'Neil, J.R., and Garcia, G.A. (1998) Effects of microbial activity on the $\delta^{18}O$ of dissolved inorganic phosphate and textural features of synthetic apatites. American Mineralogist, in press.

Canfield, D.E. and Thamdrup, B. (1994) The production of ^{34}S-depleted sulfide during bacterial disproportionation of elemental sulfur. Science, 266, 1973–1975.

Canfield, D.E., Raiswell, R., and Bottrell, S. (1992). The reactivity of sedimentary iron minerals toward sulfide. American Journal of Science, 292, 659–683.

Chambers, L.A. and Trudinger, P.A. (1979). Microbiological fractionation of stable sulfur isotopes: a review and critique. Geomicrobiology Journal, 1, 249–293.

Crowe, D.E. and Vaughan, R.G. (1996) Characterization and use of isotopically homogeneous standards for in situ laser microprobe analysis of $^{34}S/^{32}S$ ratios. American Mineralogist, 81, 187–193.

Crowe, D.E., Valley, J.W., and Baker, K.L. (1990). Microanalysis of sulfur-isotope ratios and zonation by laser microprobe. Geochimica et Cosmochimica Acta, 54, 2075–2092.

Degens, E.T. and Ittekkot, I.V. (1982). In situ metal staining of biological membranes in sediments. Nature, 298, 262–264.

Deloule, E., Allegre, C.J., and Doe, B.R. (1986) Lead and sulfur isotope microstratigraphy in galena crystals from Mississippi Valley-type deposits. Economic Geology, 81, 1307–1321.

Eldridge, C.S., Compston, W., Williams, I.S., Walshe, J.L., and Both, R.A. (1987). In situ microanalysis for $^{34}S/^{32}S$ ratios using the ion microprobe SHRIMP. International Journal of Mass Spectormetry Ion Processes, 76, 65–83.

Eldridge, C.S., Compston, W., Williams, I.S., Both, R.A., Walshe, J.L., and Ohmoto, H. (1988). Sulfur isotope variability in sediment-hosted massive sulfide deposits as determined using the ion microprobe SHRIMP: I. An example from Rammelsberg orebody. Economic Geology, 83, 443–449.

Farrand, M. (1970). Framboidal sulphides precipitated synthetically. Mineralia Deposita, 5, 237–247.

Ferris, F.G., Fyfe, W.S., and Beveridge, T.J. (1987). Bacteria as nucleation sites for authigenic minerals in a metal-contaminated lake sediment. Chemical Geology, 63, 225–232.

Fiala-Médioni, A., Pranal, V., and Colomines, J.C. (1994) Deep-sea symbiotic models chemosynthetic based: comparison of hydrothermal vents and cold seeps bivalve molluscs. Paper presented at the Proceedings of the 7th Deep-Sea Biology Symposium, IMBC, Crete.

Fisher, C.R. (1990) Chemoautotrophic and methanotrophic symbioses in marine invertebrates. CRC Critical Reviews in Aquatic Sciences, 2, 399–436.

Fortin, D., Ferris, F.G., and Beveridge, T.J. (1997) Surface-mediated mineral development by bacteria. In Mineralogical Society of America Reviews in Mineralogy, 35, 161–180.

Fossing, H. and Jørgensen, B.B. (1990). Isotope exchange reactions with radiolabeled sulfur compounds in anoxic seawater. Biogeochemistry, 9, 223–245.

Fossing, H., Thode-Andersen, S., and Jørgensen, B.B. (1992). Sulfur isotope exchange between ^{35}S-labeled inorganic sulfur compounds in anoxic marine sediments. Marine Chemistry, 38, 117–132.

Goldhaber, M.B. and Kaplan, I.R. (1980). Mechanisms of sulfur incorporation and isotope fractionation during early diagenesis in sediments of the Gulf of California. Marine Chemistry, 9, 95–143.

Goodwin, A.M., Monster, J., and Thode, H.G. (1976). Carbon and sulfur isotope abundances in Archean iron–formations and early Precambrian life. Economic Geology, 71, 870–891.

Graham, C.M. and Valley, J.W. (1991) Sulfur isotope analysis of pyrites. Chemical Geology, 101, 169–172.

Graham, U.M. and Ohmoto, H. (1994). Experimental study of formation mechanisms of hydrothermal pyrite. Geochimica et Cosmochimica Acta, 58, 2187–2202.

Greenwood, J.P., Riciputi, L.R., and McSween, H.Y. Jr. (1997). Sulfide isotopic compositions in shergottites and ALH84001, and possible implications for life on Mars. Geochimica et Cosmochimica Acta, 61, 4449–4453.

Harrison, A.G. and Thode, H.G. (1957). The kinetic isotope effect in the chemical reduction of sulphate. Transactions of the Faraday Society, 53, 1648–1651.

Kaplan, I.R., Emery, K.O., and Rittenberg, S.C. (1963). The distribution and isotopic abundance of sulphur in recent marine sediments off southern California. Geochimica et Cosmochimica Acta, 27, 297–331.

Love, L.G. (1957). Microorganisms and the presence of syngenetic pyrite. Quarterly Journal of the Geological Society of London, 113, 429–440.

Lowenstam, H.A. (1981). Minerals formed by organisms. Science, 211, 1126–1131.

Lyons, T.W. (1997) Sulfur isotopic trends and pathways of iron sulfide formation in upper Holocene sediments of the anoxic Black Sea. Geochimica et Cosmochimica Acta, 61, 3367–3382.

Lyons, T.W. and Berner, R.A. (1992) Carbon-sulfur-iron systematics of the uppermost deep-water sediments of the Black Sea. Chemical Geology, 99, 1–27.

Martin, J.B., Orange, D.L., Lorenson, T.D., and Kvenvolden, K.A. (1997) Chemical and isotopic evidence of gas-influenced flow at a transform plate boundary: Monterey Bay, California. Journal of Geophysical Research, 102, 24903–24915.

McKibben, M.A. and Eldridge, C.S. (1989). Sulfur isotopic variations among minerals and aqueous species in the Salton Sea geothermal system: a SHRIMP ion microprobe and conventional study of active ore genesis in a sediment-hosted environment. American Journal of Science, 289, 661–707.

Mohagheghi, A., Updegraff, D.M., and Goldhaber, M.B. (1985). The role of sulfate-reducing bacteria in the the deposition of sedimentary uranium ores. Geomicrobiology Journal, 4, 153–173.

Morse, J.W., Millero, F.J., Cornwell, J.C., and Rickard, D. (1987). The chemistry of the hydrogen sulfide and iron sulfide systems in natural waters. Earth Science Reviews, 24, 1–42.

Nealson, K.H. and Stahl, D.A. (1997) Microorganisms and biogeochemical cycles: what can we learn from layered microbial communities? In Mineralogical Society of America Reviews in Mineralogy, 35, 5–34.

Orange, D.L., Greene, H.G., Reed, D., Martin, J.B., McHugh, C.M., Ryan, W.B.F., Maher, N., Stakes, D., and Barry, J. (1998) Widespread fluid expulsion on a translational continental margin: mud volcanoes, fault zones, headless canyons, and aquifers in Monterey Bay, California. Geological Society of America Bulletin, in press.

Paterson, B.A., Riciputi, L.R., and McSween, H.Y.J. (1997). A comparison of sulfur isotope ratio measurement using two ion microprobe techniques, and application to analysis of troilite in ordinary chondrites. Geochimica et Cosmochimica Acta, 61, 601–610.

Price, R.T. and Shieh, Y.N. (1979). Fractionation of sulfur isotopes during laboratory synthesis of pyrite at low temperatures. Chemical Geology, 27, 245–253.

Rees, C.E., Jenkins, W.J., and Monster, J. (1978). The sulfur isotopic composition of ocean water sulphate. Geochimica et Cosmochimica Acta, 42, 377–381.

Riciputi, L.R., Cole, D.R., and Machel, H.G. (1996). Sulfide formation in reservoir carbonates of the Devonian Nisku Formation, Alberta, Canada: An ion microprobe study. Geochimica et Cosmochimica Acta, 60, 325–336.

Salamy, K. (1997) Initial report on sediment cores from Smooth Ridge, Monterey Bay. Internal report, Monterey Bay Aquarium Research Institute.

Saunders, J.A., Pritchett, M.A., and Cook, R.B. (1997) Geochemistry of biogenic pyrite and ferromanganese coatings from a small watershed: A bacterial connection? Geomicrobiology Journal, 14, 203–217.

Schneiderhöhn, H. (1923). Chalkographische Untersuchung des Mansfelder Kupferschiefers. Neues Jahrbuch. Mineralogie, Geologie, Paläeontologie, 47, 1–38.

Schoonen, M.A.A. and Barnes, H.L. (1991a). Reactions forming pyrite and marcasite from solution: I. Nucleation of FeS_2 below 100 °C. Geochimica et Cosmochimica Acta, 55, 1495–1504.

———(1991b). Reactions forming pyrite and marcasite from solution: II. Via FeS precursors below 100 °C. Geochimica et Cosmochimica Acta, 55, 1505–1514.

Shearer, C.K., Layne, G.D., Papike, J.J., and Spilde, M.N. (1996). Sulfur

isotopic systematics in alteration assemblages in martian meteorite Allan Hills 84001. Geochimica et Cosmochimica Acta, 60, 2921–2926.

Skyring, G.W. (1987). Sulfate reduction in coastal ecosystems. Geomicrobiology Journal, 5, 295–374.

Stakes, D., Orange, D., Paduan, J.B., and Maher, N. (1998) Cold-seeps and authigenic carbonate deposition in Monterey Bay, California. Marine Geology, in review.

Steineke, K. (1963). A further remark on biogenic sulfides: inorganic pyrite spheres. Economic Geology, 58, 998–1000.

Sweeney, R.E. and Kaplan, I.R. (1973). Pyrite framboid formation: Laboratory synthesis and marine sediments. Economic Geology, 68, 618–634.

Thode, H.G. and Goodwin, A.M. (1983). Further sulfur and carbon isotope studies of late Archean iron-formations of the Canadian Shield and the rise of sulfate-reducing bacteria. Precambrian Research, 20, 337–356.

von Hartmann, M. and Nielsen, H. (1969). δ^{34}S-Werte in rezenten Meeressedimenten und ihre Deutung am Beispiel einiger Sedimentprofile aus der westlichen Ostsee. Geologische Rundschau, 58, 621–655.

Wilkin, R.T. and Barnes, H.L. (1996). Pyrite formation by reactions of iron monosulfides with dissolved inorganic and organic sulfur species. Geochimica et Cosmochimica Acta, 60, 4167–4179.

———(1997). Formation processes of framboidal pyrite. Geochimica et Cosmochimica Acta, 61, 323–339.

Wilkin, R.T., Barnes, H.L., and Brantley, S.L. (1996). The size distribution of framboidal pyrite: an indicator of redox conditions. Geochimica et Cosmochimica Acta, 60, 3897–3912.

Manuscript received February 2, 1998
Manuscript accepted August 6, 1998
Paper handled by Jillian F. Banfield